RSC Advances

PAPER

View Article Online
View Journal | View Issue

Check for updates

Cite this: *RSC Adv.*, 2017, **7**, 39049

Rapid fabrication of hollow and yolk–shell α-Fe_2O_3 particles with applications to enhanced photo-Fenton reactions†

Yueheng Zhang,[a] Yang Su,[a] Yingqing Wang,[a] Jibao He,[b] Gary L. McPherson[c] and Vijay T. John *[a]

Received 13th June 2017
Accepted 1st August 2017

DOI: 10.1039/c7ra06621j

rsc.li/rsc-advances

α-Fe_2O_3 microspheres with hollow and yolk–shell (X@Fe_2O_3) morphologies are fabricated through synthesis in the confined environment of aerosol droplets. The process exploits the competitive carbonization of sucrose and the recrystallization of iron salts concurrently occurring in the droplet, to control the initial placement of iron species on the external surface or within the carbon microspheres. Upon calcination, the iron salts fuse and are oxidized to form a robust α-Fe_2O_3 shell. A partial burnoff of the carbon during calcination leads to the formation of microspheres with a core of carbon while complete burnoff leads to hollow α-Fe_2O_3 particles. Integration of ceramic nanoparticles in the precursor solution results in the inclusion of clusters of such nanoparticles in the core. The flexibility of synthesis of either hollow or yolk–shell particles makes the process amenable to the rapid fabrication of functional materials. As an example, α-Fe_2O_3 hollow microspheres show a 20-fold improvement in photo-Fenton reactivity towards the degradation of methylene blue, in comparison to commercially available materials.

Open Access Article. Published on 09 August 2017. Downloaded on 4/19/2026 7:09:20 AM.
This article is licensed under a Creative Commons Attribution 3.0 Unported Licence.

1. Introduction

Iron oxide nanomaterials are widely used in the field of water splitting,[1,2] energy storage,[3–5] gas sensors,[6,7] catalysis,[8–10] water treatment,[11] and cancer therapy.[12,13] The morphology and crystallinity of nano and microscale iron oxides have significant effects on materials properties.[9,14] Amongst recent applications are the use of multishelled Fe_2O_3 microspheres and mesoporous Fe_2O_3 nanoparticles for Li ion battery anodes,[3,7,15,16] the use of single crystalline Fe_2O_3 films for enhanced water splitting efficiency[17] and the use of high surface area Fe_2O_3 nanoparticles for the catalytic decomposition of hydrogen peroxide.[9]

In generating new functional materials with iron oxides, the fabrication of hollow structures and yolk–shell structures is of much interest. Yu and coworkers used a layer-by-layer technique to generate Fe_2O_3@C microspheres which shows excellent energy storage performance.[18] Zhao *et al.* reported the formation of novel iron oxide hollow tubes through growth on a template MnOOH nanowire which then removed through dissolution of Mn^{2+} by redox reactions.[19] A variety of methods to generate hollow and yolk–shell structures are comprehensively described in a recent review.[20]

In recent work, we have demonstrated the creation of carbon microspheres decorated with iron nanoparticles through aerosolization of a precursor solution containing a carbon source (sucrose) and a soluble iron salt ($FeCl_3 \cdot 6H_2O$) followed by passage of the aerosol droplets with an inert carrier gas through a temperature controlled furnace.[21] This aerosol based process is of promise in the fabrication of unique structured materials. During passage through the furnace, carbonization of sucrose to a carbon microsphere occurs together with crystallization of the salt. A novel aspect of this experiment is the ability to modify metal placement either on the external surface of the carbon microsphere, the interior of the microsphere or a combination of the external surface and the interior, simply by varying the furnace operating temperature. This is due to the competitive rates of carbonization and iron salt crystallization in the confined environment of an aerosol droplet.[21] Fig. 1a illustrates the aerosol set up and Fig. 1b illustrates the concepts between competitive carbonization and iron salt crystallization. Thus at lower temperatures (300–500 °C), carbonization occurs prior to complete evaporation of solvent in a droplet and thus salt crystallization occurs on the external surface of the carbon microsphere. At high temperatures (>700 °C) rapid evaporation of solvent leads to iron salt crystallization with the crystals trapped in the interior of the carbonized microsphere. At intermediate temperatures, we observe that the iron species is distributed on the external surface and in the interior.

[a]*Department of Chemical and Biomolecular Engineering, Tulane University, New Orleans, LA, 70118, USA. E-mail: vj@tulane.edu*

[b]*Coordinated Instrumentation Facility, Tulane University, New Orleans, LA, 70118, USA*

[c]*Department of Chemistry, Tulane University, New Orleans, LA, 70118, USA*

† Electronic supplementary information (ESI) available. See DOI: 10.1039/c7ra06621j

Open Access Article. Published on 09 August 2017. Downloaded on 4/19/2026 7:09:20 AM.
This article is licensed under a Creative Commons Attribution 3.0 Unported Licence.

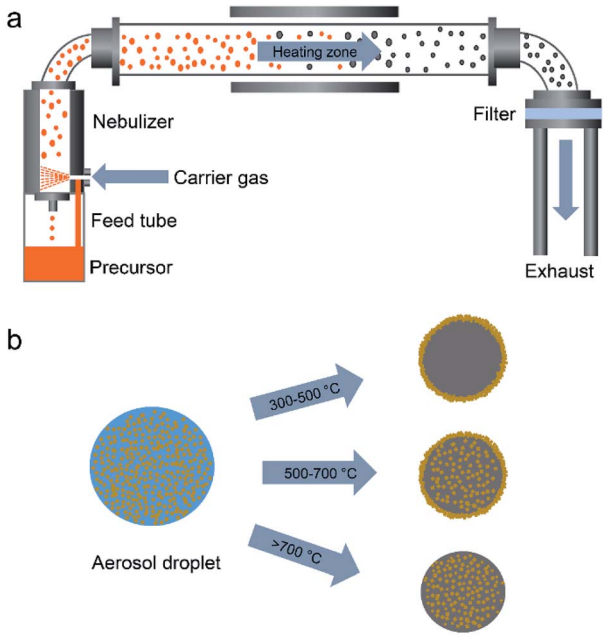

Fig. 1 (a) Schematic of the aerosol based process for microsphere synthesis. The precursor solution is first nebulized into aerosol droplets which are carried by an inert gas through the heating zone. The solvent evaporation and chemical reactions within the droplet lead to solid particle formation. The particles are further separated by a polycarbonate filter through which the carrier gas is vented. (b) Schematic illustrating the role of furnace temperature in the competitive carbonization of sucrose and the recrystallization of iron salts upon solvent evaporation.

In this paper, we primarily focus on the system where the iron salt decorates carbon microsphere and seek to understand the structure and morphology of the iron species as the carbon microsphere is progressively calcined away. Our results indicate the fusion of the iron oxide formed by calcination in air, leading to the generation of intact shells of the iron oxide containing shrunken cores of carbon that are eventually burnt off leaving hollow particles. The facile fabrication of such yolk–shell particles with a carbon core or entirely hollow iron oxide particles is a specific focus of this work. In addition, we show that the process is amenable to inclusion of other nanoparticles into the voids of the hollow particles, indicating methods to produce new multifunctional particles. Finally, the application of these materials to a photocatalyzed Fenton type reaction is demonstrated.

2. Experimental

2.1. Materials

Iron chloride hexahydrate ($FeCl_3 \cdot 6H_2O$, 97%, ACS reagent), sucrose ($C_{12}H_{22}O_{11}$, ACS reagent), hydrogen peroxide (H_2O_2, 30%), iron oxide nanopowder, and methylene blue (MB) were purchased from Sigma-Aldrich. Colloidal silica with a diameter of 100 nm was provided by Nissan Chemical Company. Coumarin and 7-hydroxycoumarin used in this study were purchased from Sigma Aldrich and Alfa Aesar respectively. All chemicals were used as received.

2.2. Preparation of iron oxide microsphere with a hollow structure

The first step of the synthesis procedure is based on the formation of carbon microspheres with surface crystallization of iron salts through an aerosol based process, following our earlier procedure.[21] Thus, the aerosol precursor solution was prepared by dissolving 2.0 g sucrose and 2.0 g $FeCl_3 \cdot 6H_2O$ in 7.5 mL deionized water. The solution was magnetically stirred for 30 min and was then aerosolized into droplets by an inexpensive nebulizer (Micro Mist, TeleFlex Inc.) with a jet hole diameter of 1 mm. The aerosol droplets were carried by nitrogen to pass through a tube furnace (MTI, GSL-1100X) using a quartz tube (100 cm length × 4.5 cm diameter, with 66 cm of the tube being in the furnace). The flow rate of nitrogen was set to 6.5 L min^{-1}, leading to a furnace residence time of 8.6 s. Fig. 1 in the text shows the schematic of the process with the solid product exiting the furnace being collected by a filter with pore size of 0.22 μm (Merck Millipore Ltd.). The temperature of the filter plate was maintained at 100 °C to prevent condensation of the solvent. The as-synthesized microspheres were further calcined in air at 400 °C for 3 hours to remove any carbon residues.

2.3. Encapsulation of guest particles in the hollow microspheres

The encapsulation of ceramic nanoparticles (SiO_2) simply involved including the nanoparticles as a suspension in the aerosol precursor solution described above. SiO_2@Fe_2O_3 yolk–shell microspheres were formed after calcination in air at 400 °C for 3 hours.

2.4. Characterization

Scanning electron microscopy (SEM) was conducted using a Hitachi S-4800 instrument with an accelerating voltage of 10 kV to characterize surface morphology of the microsphere. The sample was sputter coated with an ultrathin gold layer to enhance surface conductivity. Transmission electron microscopy (TEM) was done using an FEI G2F30 Tecnai TEM operating at 300 kV. Cross-sectional TEM was also carried out to characterize the inner structure of the microsphere. The microspheres were immersed in an epoxy resin precursor, and the mixture was allowed to cure at 80 °C for 2 days. The resin with particles embedded was then cut into 70 nm slices using a microtome. The sample was transferred to a copper grid and observed under the TEM. X-ray diffraction (XRD) patterns were obtained on a Rigaku MiniFlexII Diffractometer (Cu Kα radiation, λ = 1.54 Å). The X-ray photoelectron spectroscopy (XPS) was done on a VG Scientific MKII system using an Al Kα anode as excitation source ($h\nu$ = 1486.6 eV). The pressure in the chamber during the analysis was $<5 \times 10^{-8}$ mbar.

2.5. Photocatalytic degradation of MB

The photocatalytic degradation of MB was investigated by mixing 10 mL of the dye solution (14 mg L^{-1}) with 10 mg Fe_2O_3 hollow microsphere.[22] The mixture was stirred to ensure uniform dispersion of the microspheres. The mixture was kept

 This journal is © The Royal Society of Chemistry 2017

Open Access Article. Published on 09 August 2017. Downloaded on 4/19/2026 7:09:20 AM.
This article is licensed under a Creative Commons Attribution 3.0 Unported Licence.

stirred for 1 hour before the addition of 0.1 mL hydrogen peroxide (30%, H_2O_2) and exposure to UV irradiation to allow dye adsorption equilibrium. The sample was irradiated at 395 nm using a 24 W lamp. 400 μL aliquots of the irradiated sample were taken at various sampling times, diluted 3 times and the UV-Vis absorbance scans were done using a Shimadzu, UV1700 instrument. The $^{\bullet}OH$ produced during the photo-Fenton reaction was monitored using coumarin as a scavenger.[23,24] The production of 7-hydroxycoumarin was monitored using PTI Felix 32 MD-5020 spectrofluorimeter.

3. Results and discussion

3.1. Formation of α-Fe_2O_3 hollow microspheres

Fig. 1a illustrates the setup of the aerosol based process.[25] Briefly, the solution of sucrose and $FeCl_3 \cdot 6H_2O$ was nebulized into aerosol droplets which were further heated up during passage in the tube furnace to form micron and submicron sized particles. The aerosol droplets undergo solvent evaporation, sucrose carbonization, and precipitation of iron salts when passing through the heating zone, leading to the formation of a black powder of iron salt/carbon composites. Fig. 1b is a schematic of results from our earlier work[21] where we demonstrated that furnace operation at lower temperature leads to particles with iron species on the external surface of the carbon microspheres formed through carbonization in aerosol droplets, while operation at high temperatures leads to iron species being integrated into the carbon microspheres. At intermediate temperatures, the iron species are distributed both on the surface and within the carbon microspheres.[21]

We focus here on the lower temperature process of deposition of iron salts on the surface of the carbon microsphere as this is the route to the production of hollow particles. Fig. 2 shows a typical morphology of the as-synthesized carbon microspheres. The SEM image (Fig. 2a) illustrates a smooth surface that is verified in the image of the circumferential edge of another particle observed through TEM (Fig. 2b). However, a cross-section TEM image (Fig. 2c) reveals a darker circumferential edge pointing out the existence of iron species which gives a higher image contrast under the electron beam than the carbonaceous core and the resin matrix used to embed the particles. The XRD pattern (Fig. 2d) of the iron salt on the surface shows the predominance of $FeCl_2 \cdot H_2O$ indicating the reduction of Fe^{3+} to Fe^{2+} during the aerosolization and deposition on carbon. Additional iron species as shown by the smaller peaks of the X-ray diffractogram are difficult to clearly identify. We also note that there is an inherent polydispersity to particle size (inset to Fig. 2a) when synthesized through the aerosol process which can be minimized through the use of finer nozzles *etc.* Fig. 2e is a scanning transmission electron micrograph (STEM) of the particles in Fig. 2b, and the presence of a ring in Fig. 2b and e may also be a consequence of the surface coating of the iron salt. EELS spectra of Fe (Fig. 2f) and Cl (Fig. 2g) and the merged spectra (Fig. 2h) indicate a relatively uniform surface distribution of the two elements on the microsphere surface.

To produce hollow particles, the as-synthesized microspheres were further calcined in air at 400 °C for 3 hours and the structures characterized using SEM, TEM, cross-sectional TEM and XRD (Fig. 3). From the SEM image (Fig. 3a), we see that the structures retain spherical morphologies but that the surface

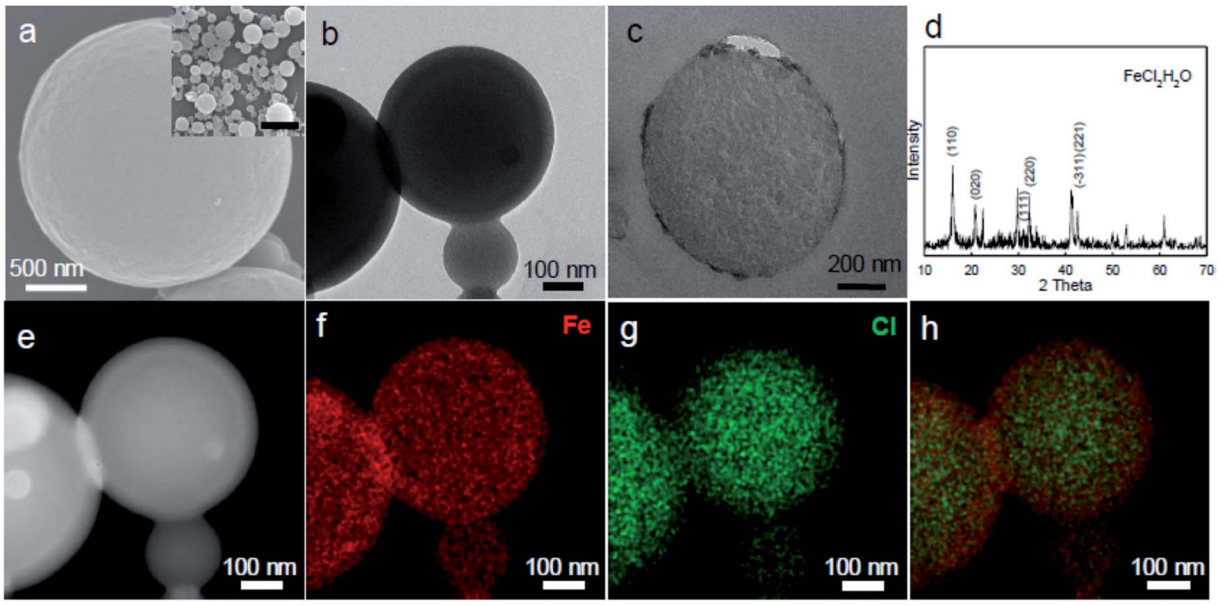

Fig. 2 (a) Scanning electron micrograph (SEM) of the as synthesized particles at 300 °C before calcination. The inset to (a) shows multiple particles to demonstrate the size polydispersity inherent in the aerosol process. The scale bar is 5 μm. (b) Transmission electron micrograph (TEM) of the same batch of particles. (c) Cross-sectional TEM of the same batch of particles. (d) X-ray diffractogram (XRD) of the particles to show the presence of $FeCl_2$. (e) Scanning transmission electron micrograph (STEM) of the same batch of particles. (f–h) Electron energy loss spectroscopy (EELS) elemental mapping showing Fe (f), Cl (g) and the merged distribution (h). Both elements are relatively uniformly distributed.

Open Access Article. Published on 09 August 2017. Downloaded on 4/19/2026 7:09:20 AM.
This article is licensed under a Creative Commons Attribution 3.0 Unported Licence.

becomes rough through the formation of nanocrystals that are 50–100 nm. The TEM image (Fig. 3b) reveals that calcination in air at these conditions transforms the solid microspheres into hollow microspheres. The shell has a thickness of around 50–100 nm suggesting that the shell consists of a single layer of particulates. This is confirmed by the cross-sectional TEM image of Fig. 3c. The crystallographic structure of the nanocrystallites was determined by XRD. All peaks are matched to the α-Fe_2O_3 phase (JCPDS card no. 33-0664), indicating complete oxidation of the iron species to α-Fe_2O_3 during calcination. We note that at 400 °C, complete burnoff of the carbon and the production of hollow microspheres can be obtained in as little as 10–15 min.

To understand the formation of the hollow structure of the microspheres, we used TEM to track the morphological changes of the microsphere upon calcination (Fig. 4). The as-synthesized microspheres were heated up to 325 °C, 350 °C and 400 °C in air successively at a temperature ramp rate of 5 °C min^{-1}, with a 5 minute isotherm preceding each ramp to allow sampling for TEM imaging. Sampling at 325 °C, reveals a partially burnt-off carbon core (Fig. 4a). The remarkable aspect of the carbon burn-off is the fusion of the iron species and the retention of the iron rich shell. We thus observe a progressively shrinking carbon core (images Fig. 4b and c) as also schematically shown in Fig. 4d eventually leading to the hollow microparticle morphology. We note from the cross-sectional TEM that there is no evidence of Fe_2O_3 within the shell. However, it is possible to generate Fe_2O_3 clusters within shell using the mechanism of iron salt initial placement as shown in Fig. 1b. Thus operation at higher operating temperature (600 °C) leads to a distribution of iron both on the surface and within the carbon particles.

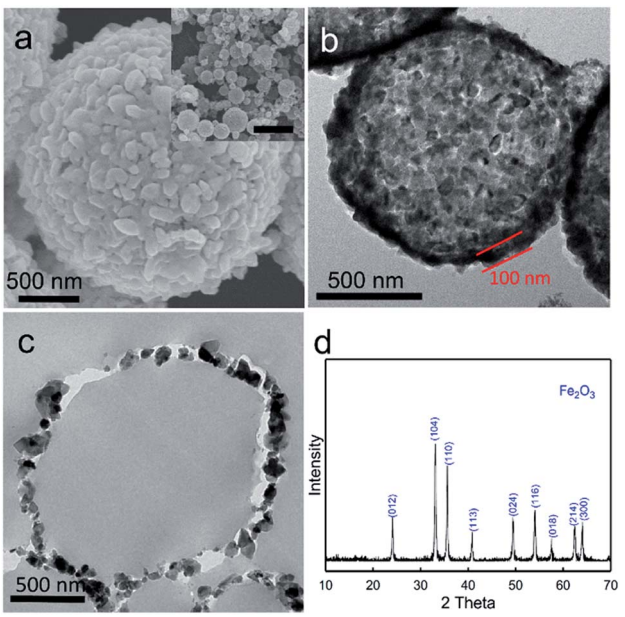

Fig. 3 (a–d) SEM, TEM, cross-sectional TEM and XRD pattern of the α-Fe_2O_3 hollow microspheres formed by synthesis at 300 °C followed by calcination at 400 °C for 3 hours. We note the α-Fe_2O_3 crystallite size in the shell is approximately 50 nm. The scale bar of inset in a is 5 μm.

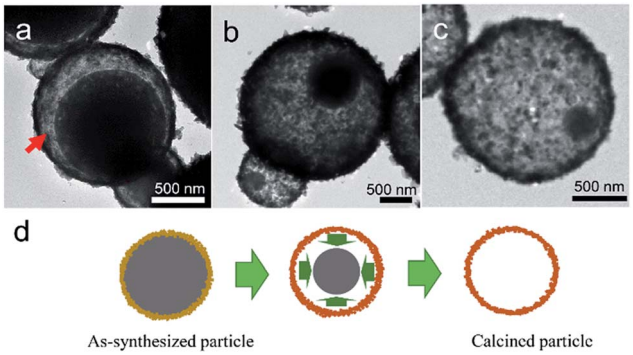

Fig. 4 Structural evolution of the particle during calcination. The temperature was ramped successively to 325, 350 and 400 °C at 5 °C min^{-1} in air. Following each temperature, a 5 min isothermal step was allowed for sampling. (a–c) TEM images of particles heated to 325, 350, 400 °C. (d) Schematic of the formation of hollow iron oxide microspheres correlating to the TEM images. The Fe_2O_3 shell forms first and is robust during the remaining burnoff of the carbon to generate the hollow Fe_2O_3 particles.

When such composite particles are calcined, we observe clear evidence of particles with a Fe_2O_3 shell and a sintered cluster of Fe_2O_3 nanoparticles (Fig. 5). The observations point to the importance of initial iron salt placement, and complement multistep methods using presynthesized carbon microspheres followed by adsorption of iron particles.[15]

To summarize, the formation of hollow α-Fe_2O_3 microparticles is based on the competition between sucrose carbonization and iron salt precipitation in the confined environment of aerosol microdroplets. At the aerosolization temperatures used (300 °C), carbonization occurs first, followed by the enrichment and recrystallization of iron salts onto the carbon external surface as the remnant solvent evaporates off. During the calcination step, the iron species on the external surface of the carbon are oxidized to α-Fe_2O_3 crystallites. These crystallites aggregate and fuse rapidly to create a robust shell that is intact while the carbonaceous core is gradually burnt off. The morphology of the Fe/carbon composite which is controlled by the temperature of the heating zone the droplets pass through, is highly relevant to the resulting α-Fe_2O_3 morphology. Pioneering work by Zhou and coworkers[26] is complementary to our observations as they report the encapsulation of α-Fe_2O_3 in a carbon matrix through a relatively lower temperature (220 °C) aerosolization where the carbonization is slow enough to allow integration of the iron salt.

3.2. Applications to photo-Fenton type reactions for environmental remediation

To translate these iron oxide morphologies to a specific application, we used the degradation of methylene blue (MB – methylthionium chloride) through photoenhanced Fenton type mechanisms as a model reaction. MB is a widely used dye in printing, textile, and many other industries.[27,28] The release of waste water containing MB leads to anoxic pollution and is harmful to aquatic organisms.[27,29] While treatment methods involving absorption, biodegradation, and chlorination have

 This journal is © The Royal Society of Chemistry 2017

Open Access Article. Published on 09 August 2017. Downloaded on 4/19/2026 7:09:20 AM.
This article is licensed under a Creative Commons Attribution 3.0 Unported Licence.

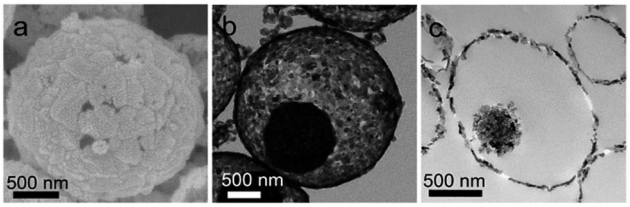

Fig. 5 (a–c) SEM, TEM, and cross-sectional TEM images of microspheres with a yolk–shell structure, synthesized at 600 °C followed by calcination at 400 °C for 3 hours. We note the higher temperature of synthesis leads to Fe_2O_3 clusters within the Fe_2O_3 shell.

been extensively studied, the effective treatment of MB contaminated wastewater remains challenging.[30] Heterogeneous Fenton type reactions to oxidize MB may be effective.[31–33] Iron oxide can activate H_2O_2 and generate $^{\bullet}OH$ radicals to degrade MB (eqn (1)–(3)),[34] but the reaction is hampered by slow kinetics. However, by coupling with UV irradiation, the heterogeneous Fenton type reaction can be accelerated.[22,31,35,36] Nanocrystalline α-Fe_2O_3 has a band gap of 2.2 eV,[37] with generation of electron–hole pairs through irradiation at wavelengths less than 564 nm. The photo-enhanced Fenton mechanism is shown through eqn (4)–(8) below.[35,38,39]

$$Fe(III)_{surf} + H_2O_2 \rightarrow Fe(III)_{surf}(H_2O_2) \quad (1)$$

$$Fe(III)_{surf}(H_2O_2) \rightarrow Fe(II)_{surf} + HO_2^{\bullet} + H^+ \quad (2)$$

$$Fe(II)_{surf} + H_2O_2 \rightarrow Fe(III)_{surf} + {}^{\bullet}OH + HO^- \quad (3)$$

$$Fe_2O_3(s) + h\nu \rightarrow Fe_2O_3\,(e^- + h^+) \quad (4)$$

$$h^+ + H_2O \rightarrow {}^{\bullet}OH + H^+ \quad (5)$$

$$e^- + Fe(III)_{surf} \rightarrow Fe(II)_{surf} \quad (6)$$

$$MB + h\nu \rightarrow MB^* \quad (7)$$

$$Fe(III)_{surf} + MB^* \rightarrow Fe(II)_{surf} + HO_2^{\bullet} + H^+ \quad (8)$$

In the equations above, $Fe(II)_{surf}$ and $Fe(III)_{surf}$ in the equations are iron species at the surface of the iron oxide. Fig. 6a illustrates the absorbance spectra of irradiated MB catalyzed by Fe_2O_3 hollow microspheres in the presence of H_2O_2 at 10 min intervals, with the kinetics of degradation based on the loss of intensity at 664 nm. The use of a first-order reaction to model kinetics works extremely well (Fig. 6b) allowing the calculation of pseudo first order rate constants. As a comparison, MB degradation reactivity was tested with commercially available α-Fe_2O_3 nanoparticles with and without light irradiation, respectively. As shown in Fig. 6b, $\ln(C/C_0)$ shows a linear dependence on the reaction time, indicating applicability of pseudo-first order kinetics. The reaction rate constant is 8.05 g^{-1} min^{-1} for the system with hollow microspheres which is significantly larger than the corresponding rate constants for the other systems validating both the photo-Fenton enhanced reaction and the use of the hollow microspheres. Our hypothesis is that such hollow microspheres

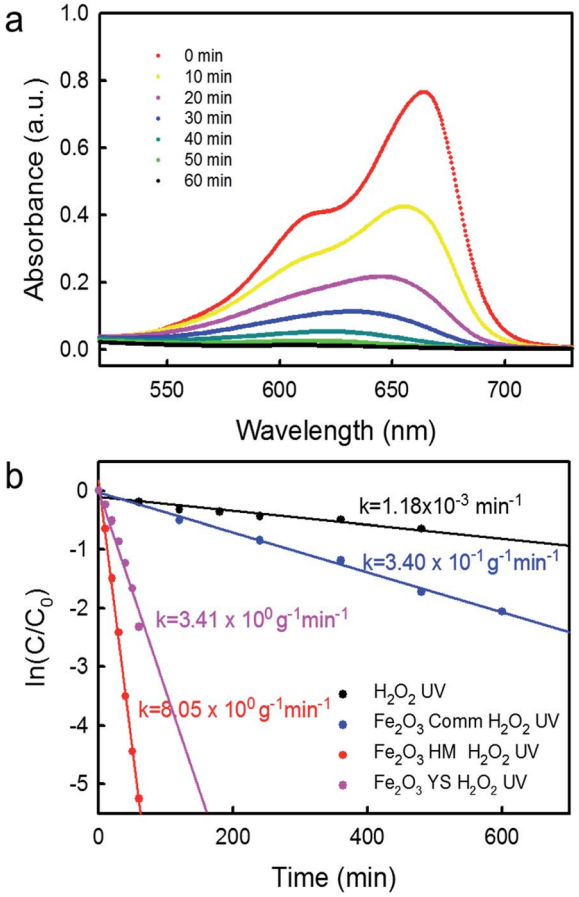

Fig. 6 Enhanced photocatalytic degradation of methylene blue with α-Fe_2O_3 hollow microspheres. (a) Time dependent UV-Vis spectra for the photocatalytic degradation of MB with α-Fe_2O_3 hollow microspheres (HM) under irradiation at 395 nm. (b) Comparison of reaction constants of degradation of MB with three systems: H_2O_2 + commercial Fe_2O_3, H_2O_2 + commercial Fe_2O_3 + UV, H_2O_2 + Fe_2O_3 hollow microspheres (HM) + UV, and H_2O_2 + Fe_2O_3 yolk–shell (YS) microspheres + UV. All rate constants are normalized based on the weight of Fe_2O_3 used.

allowing light irradiation to penetrate to the interior might result in a greater rate of hydroxyl radical generation through the reduction of $Fe(III)_{surf}$ to $Fe(II)_{surf}$ (eqn (6) above) enhancing the reaction rate. While the classic Fenton reaction requires the pH to be maintained in a narrow range (2–4), the heterogeneous photo-Fenton reaction is less sensitive to pH values due to UV induced redox cycling between Fe(II) and Fe(III).[9,31,39] Fig. S1 in the ESI† shows the change in pH with time showing a drop in pH from 7.8 initially to 5.4 for the most reactive α-Fe_2O_3 hollow microsphere system. This is due to the acidic intermediates generated from MB degradation and the final evolution of CO_2 and H_2O.[40] Quantitative determination of the hydroxyl radical generation through the photo-Fenton reaction on the hollow Fe_2O_3 done using coumarin as a scavenger[23] showed the generation of about 0.2 μM min^{-1} $^{\bullet}OH$ radicals (ESI S2†). We also note that the narrow band gap of 2.2 eV for Fe_2O_3 implies that the reaction can be done with illumination less than 570 nm.

Open Access Article. Published on 09 August 2017. Downloaded on 4/19/2026 7:09:20 AM.
This article is licensed under a Creative Commons Attribution 3.0 Unported Licence.

3.3. Inclusion of other species and the fabrication of X@Fe_2O_3 microspheres

The flexibility of the hollow microsphere fabrication allows the introduction of increased structural complexity to enhance functionality. Since the first step involves synthesis in the confined medium of an aerosol droplet, it is possible to incorporate other colloidally suspended materials in the precursor solution which inherently become encapsulated in the aerosol droplet. The objective therefore is to determine if the final Fe_2O_3 microsphere is able to encapsulate such species. As a specific example, we sought to demonstrate the encapsulation of 100 nm SiO_2 colloidal nanoparticles in Fe_2O_3 to form SiO_2@Fe_2O_3 microspheres. The concentration of the SiO_2 suspension used in the experiment was 40% by weight. The final weight ratio of the precursor composition was sucrose : $FeCl_3 \cdot 6H_2O$: $SiO_2 = 1 : 1 : 0.2$. The precursor solution was aerosolized into droplets to pass through the 300 °C heating zone. The as-synthesized microspheres were calcined in air at 400 °C. The microspheres before and after calcination were characterized by SEM, TEM, and cross-sectional TEM (Fig. 7).

As shown in the SEM and TEM images of the as-synthesized microspheres (Fig. 7a and b), microspheres with smooth surfaces are formed, but no SiO_2 nanoparticles are observed on the surface of the microspheres. The cross-sectional TEM image (Fig. 7c) reveals that SiO_2 nanoparticles are embedded in the carbon matrix. We thus observe thermally stable nanoparticles such as SiO_2 becoming incorporated into the carbon microsphere matrix upon aerosolization and passage through the furnace at these temperatures. Fig. 7d–f show the fate of these composite particles after calcination to remove carbon and fuse the iron oxide to form the hollow Fe_2O_3 microspheres. Fig. 7d illustrates the SEM image of the external surface of the Fe_2O_3 crystallites. The TEM image of Fig. 7e illustrates the presence of a core in the hollow interior which is further resolved through the cross-sectional TEM image of Fig. 7f to clearly show 100 nm SiO_2 nanoparticles. XPS characterizations of these SiO_2@Fe_2O_3 particles (ESI S3†) further indicate the encapsulation of SiO_2 within the α-Fe_2O_3 hollow particles.

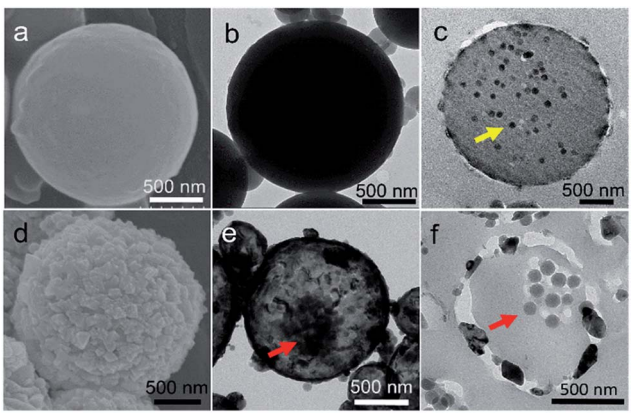

Fig. 7 (a–c) SEM, TEM, and cross-sectional TEM images of microspheres synthesized at 300 °C with SiO_2 nanoparticles dispersed in the precursor. Before calcination, SiO_2 nanoparticles are embedded within the carbonaceous matrices (yellow arrow of (c)), but no SiO_2 nanoparticles are observed on the surface of the microspheres. (d–f) SEM, TEM, and cross-sectional TEM images of SiO_2@Fe_2O_3 microspheres. After calcination, SiO_2@Fe_2O_3 microspheres are formed with the cluster of silica nanoparticles as the core (red arrows in (e and f)) and Fe_2O_3 as the shell.

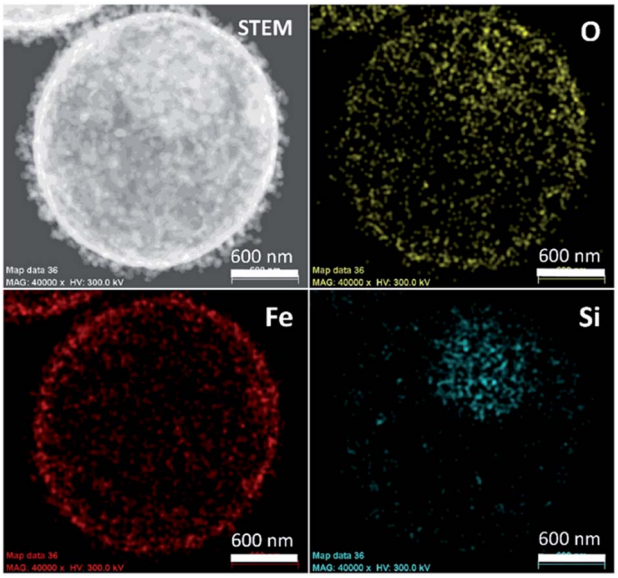

Fig. 8 STEM image and element mapping images of SiO_2@Fe_2O_3 microspheres. The element distribution verifies the presence of a SiO_2 nanoparticle cluster in a shell of α-Fe_2O_3.

Fig. 8 shows the STEM image and the element mapping of a typical individual calcined microsphere. The O signal shows an increased concentration in the first quadrant of the image due to contributions from both α-Fe_2O_3 and SiO_2 as the Si signal is primarily confined to the first quadrant. The Fe signal appears to be uniformly distributed over the surface of the microsphere. We conclude that the SiO_2 exists as a cluster of nanoparticles perhaps fused by Si–O–Si bonds. Nevertheless, these results confirm the ability to successfully encapsulate SiO_2 within the α-Fe_2O_3 microsphere SiO_2@Fe_2O_3 yolk–shell microsphere. The formation of the SiO_2@Fe_2O_3 yolk–shell microsphere is also tracked by sampling the microspheres during the calcination and carbon burnoff. The shell forms at 325 °C and continuous shrinking of the carbon results in the aggregation of SiO_2 nanoparticles form a cluster as the core (data not shown). Extensions to other functional nanoparticles (*e.g.* TiO_2) are inherent in these observations.

4. Conclusions

To summarize, we have demonstrated a facile and rapid method to fabricate hollow α-Fe_2O_3 microspheres and yolk–shell particles through synthesis in the confined geometry of aerosol droplets. There are specific aspects of novelty to the work. First, a clear mechanism of competitive carbonization and iron salt crystallization is exploited to derive the hollow particles or particles containing a proposed formation mechanism of the hollow structure involves carbonization of sucrose

This journal is © The Royal Society of Chemistry 2017

Open Access Article. Published on 09 August 2017. Downloaded on 4/19/2026 7:09:20 AM.
This article is licensed under a Creative Commons Attribution 3.0 Unported Licence.

within a droplet to form carbon microspheres, followed by precipitation of iron salts onto the external surface of the microsphere. Calcination to burn off the microspheres results in the formation of fused α-Fe_2O_3 microcrystallites that are robust and maintain structure throughout the calcination. Partial burnoff of carbon through a shrinking core mechanism leads to small microspheres of carbon embedded in a shell of α-Fe_2O_3. Total burnoff of carbon leads to an entirely hollow microsphere of α-Fe_2O_3. Furthermore, we have demonstrated that this aerosol based synthesis route can be used to fabricate X@Fe_2O_3 microspheres where X denotes colloidally stable nanoparticles such as SiO_2 or TiO_2. Our results therefore indicate a new convenient way to fabricate hollow structures and subsequent yolk–shell structures without the scale-up issues inherent in traditional templating techniques.

As an example of a relevant application, we have shown that the α-Fe_2O_3 microspheres have a high activity in photo-enhanced Fenton reactions with reaction rates that are an order of magnitude higher than commercial α-Fe_2O_3 particles for the decontamination of methylene blue. We propose that the enhancement in kinetics is due to the ability of the hollow structures both to trap and increase contact times for the reactants and to allow multiple light reflections from the hollow interior to increase the photocatalytic yield. Further studies are underway to translate the findings to relevant environmental decontamination reactions.

The method of particle preparation, especially the capability to fabricate hybrid microspheres, is clearly applicable to a wide range of technologies besides the photo-Fenton reaction. Pioneering recent work by Yu and coworkers[41,42] and by Kang and coworkers[43] has shown the application of such materials in fabricating anode materials for Li-ion batteries. Zhou and coworkers have shown the remarkable aspect of α-Fe_2O_3 encapsulation in graphitic carbon microspheres through essentially a low temperature aerosolization process.[26] Hybrid particles with α-Fe_2O_3 as the core component and SnO_2 as the shell have also shown promising application potential to energy storage.[44] Integration of Si nanoparticles in the carbon-based structures will allow these materials to be used in Li-ion battery technology taking advantage of the ability of both Si and α-Fe_2O_3 to encapsulate Li ions. Such studies are also the focus of continuing work.

Acknowledgements

Support by the National Science Foundation (Grant 1236089) is gratefully acknowledged.

References

1 A. Kay, I. Cesar and M. Grätzel, *J. Am. Chem. Soc.*, 2006, **128**, 15714–15721.
2 G. Wang, Y. Ling, D. A. Wheeler, K. E. N. George, K. Horsley, C. Heske, J. Z. Zhang and Y. Li, *Nano Lett.*, 2011, **11**, 3503–3509.
3 Y. Xu, G. Jian, Y. Liu, Y. Zhu, M. R. Zachariah and C. Wang, *Nano Energy*, 2014, **3**, 26–35.
4 L. Zhang, H. B. Wu, S. Madhavi, H. H. Hng and X. W. Lou, *J. Am. Chem. Soc.*, 2012, **134**, 17388–17391.
5 N. Zhang, X. Han, Y. Liu, X. Hu, Q. Zhao and J. Chen, *Adv. Energy Mater.*, 2015, **5**, 1401123.
6 L. H. Huo, X. L. Li, W. Li and S. Q. Xi, *Sens. Actuators, B*, 2000, **71**, 77–81.
7 J. Chen, L. Xu, W. Li and X. Gou, *Adv. Mater.*, 2005, **17**, 5.
8 P. Li, D. E. Miser, S. Rabiei, R. T. Yadav and M. R. Hajaligol, *Appl. Catal., B*, 2003, **43**, 151–162.
9 M. Hermanek, R. Zboril, I. Medrik, J. Pechousek and C. Gregor, *J. Am. Chem. Soc.*, 2007, **129**, 10929–10936.
10 X. Mou, B. Zhang, Y. Li, L. Yao, X. Wei, D. S. Su and W. Shen, *Angew. Chem., Int. Ed.*, 2012, **51**, 2989–2993.
11 L. S. Zhong, J. S. Hu, H. P. Liang, A. M. Cao, W. G. Song and L. J. Wan, *Adv. Mater.*, 2006, **18**, 2426–2431.
12 H. Fan, J. B. Yi, Y. Yang, K. Kho, X. W. Sun, M. C. Olivo and Y. P. Feng, *ACS Nano*, 2009, **3**, 11.
13 X.-H. Peng, X. Qian, H. Mao, A. Y. Wang, Z. Chen, S. Nie and D. M. Shin, *Int. J. Nanomed.*, 2008, **3**, 311–321.
14 J. H. Bang and K. S. Suslick, *J. Am. Chem. Soc.*, 2007, **129**, 2242–2243.
15 S. M. Xu, C. M. Hessel, H. Ren, R. B. Yu, Q. Jin, M. Yang, H. J. Zhao and D. Wang, *Energy Environ. Sci.*, 2014, **7**, 632–637.
16 B. Wang, J. S. Chen, H. B. Wu, Z. Wang and X. W. Lou, *J. Am. Chem. Soc.*, 2011, **133**, 17146–17148.
17 C. Jorand Sartoretti, B. D. Alexander, R. Solarska, I. A. Rutkowska, J. Augustynski and R. Cerny, *J. Phys. Chem. B*, 2005, **109**, 13685–13692.
18 H. Zhang, L. Zhou, O. Noonan, D. J. Martin, A. K. Whittaker and C. Yu, *Adv. Funct. Mater.*, 2014, **24**, 4337–4342.
19 K. Zhao, M. Wen, Y. Dong, L. Zhang, M. Yan, W. Xu, C. Niu, L. Zhou, Q. Wei, W. Ren, X. Wang and L. Mai, *Adv. Energy Mater.*, 2017, **7**, 1601582–1602591.
20 L. Zhou, Z. Zhuang, H. Zhao, M. Lin, D. Zhao and L. Mai, *Adv. Mater.*, 2017, **29**, 1602914–1602943.
21 B. Sunkara, J. Zhan, I. Kolesnichenko, Y. Wang, J. He, J. E. Holland, G. L. McPherson and V. T. John, *Langmuir*, 2011, **27**, 7854–7859.
22 A. M. Mansour, *RSC Adv.*, 2015, **5**, 62052–62061.
23 Q. Xiang, J. Yu and P. K. Wong, *J. Colloid Interface Sci.*, 2011, **357**, 163–167.
24 H. Czili and A. Horváth, *Appl. Catal., B*, 2008, **81**, 295–302.
25 J. Zhan, I. Kolesnichenko, B. Sunkara, J. He, G. L. McPherson, G. Piringer and V. T. John, *Environ. Sci. Technol.*, 2011, **45**, 1949–1954.
26 H. Zhang, X. Sun, X. Huang and L. Zhou, *Nanoscale*, 2015, **7**, 3270–3275.
27 A. Houas, H. Lachheb, M. Ksibi, E. Elaloui, C. Guillard and J.-M. Herrmann, *Appl. Catal., B*, 2001, **31**, 145–157.
28 M. Rafatullah, O. Sulaiman, R. Hashim and A. Ahmad, *J. Hazard. Mater.*, 2010, **177**, 70–80.
29 Z. Zhang and J. Kong, *J. Hazard. Mater.*, 2011, **193**, 325–329.
30 A. K. Dutta, S. K. Maji and B. Adhikary, *Mater. Res. Bull.*, 2014, **49**, 28–34.
31 P. V. Nidheesh, *RSC Adv.*, 2015, **5**, 40552–40577.

Open Access Article. Published on 09 August 2017. Downloaded on 4/19/2026 7:09:20 AM.
This article is licensed under a Creative Commons Attribution 3.0 Unported Licence.

32 E. G. Garrido-Ramírez, B. K. G. Theng and M. L. Mora, *Appl. Clay Sci.*, 2010, **47**, 182–192.
33 S. Navalon, M. Alvaro and H. Garcia, *Appl. Catal., B*, 2010, **99**, 1–26.
34 W. P. Kwan and B. M. Voelker, *Environ. Sci. Technol.*, 2003, **37**, 1150–1158.
35 X. Yang, W. Chen, J. Huang, Y. Zhou, Y. Zhu and C. Li, *Sci. Rep.*, 2015, **5**, 10632.
36 M. Hartmann, S. Kullmann and H. Keller, *J. Mater. Chem.*, 2010, **20**, 9002–9017.
37 A. Duret and M. Grätzel, *J. Phys. Chem. B*, 2005, **109**, 17184–17191.
38 W. Du, Y. Xu and Y. Wang, *Langmuir*, 2008, **24**, 175–181.
39 C. Wang, H. Liu and Z. Sun, *Int. J. Photoenergy*, 2012, **2012**, 10.
40 Q. Wang, S. Tian and P. Ning, *Ind. Eng. Chem. Res.*, 2014, **53**, 643–649.
41 Z. Padashbarmchi, A. H. Hamidian, H. Zhang, L. Zhou, N. Khorasani, M. Kazemzad and C. Yu, *RSC Adv.*, 2015, **5**, 10304–10309.
42 L. Zhou, H. Xu, H. Zhang, J. Yang, S. B. Hartono, K. Qian, J. Zou and C. Yu, *Chem. Commun.*, 2013, **49**, 8695–8697.
43 M. Y. Son, Y. J. Hong, J. K. Lee and Y. Chan Kang, *Nanoscale*, 2013, **5**, 11592–11597.
44 J. S. Chen, C. M. Li, W. W. Zhou, Q. Y. Yan, L. A. Archer and X. W. Lou, *Nanoscale*, 2009, **1**, 280–285.

This journal is © The Royal Society of Chemistry 2017